NAG 8-457

The Pennsylvania State University

The Graduate School

Department of Astronomy

X-ray Inverse Compton Emission From the Radio Halo of M87

A Thesis in

Astronomy

by

Perry Alan David Wood

Submitted in Partial Fulfillment
of the Requirements
for the Degree of

Master of Science

May 1985

Perry A. D. Wood
Perry Alan David Wood

We approve the thesis of Perry Alan David Wood.

Date of Signature:

1 March 85 — Eric D. Feigelson

Eric D. Feigelson, Assistant Professor of Astronomy, Thesis Adviser

1 Mar 85 — Gordon P. Garmire

Gordon P. Garmire, Professor of Astronomy

1 Mar 85 — S. Matsushima

Satoshi Matsushima, Professor of Astronomy, Head of the Department of Astronomy

1 March 85 — Daniel W. Weedman

Daniel W. Weedman, Professor of Astronomy

ABSTRACT

M87 has been observed in the 0.2-4 KeV X-ray band using the High Resolution Imager on the Einstein Observatory, and at 1.452 GHz using the Very Large Array. The radio map showed that the halo contained prominent asymmetries to the east and southwest. The X-ray map indicated similar asymmetries, but they were imbedded in the diffuse hot gas that surrounds the core out to a radius of several arcminutes. The hot X-ray emitting gas was assumed to be spherically symmetric and could, therefore, be subtracted from the image. The resultant image was asymmetric with major lobes to the east and southwest that coincide approximately with the asymmetries in the radio halo. The data indicates that inverse Compton emission is a plausible model for the X-rays coming from the asymmetric component.

TABLE OF CONTENTS

LIST OF TABLES

LIST OF FIGURES

ACKNOWLEDGEMENTS

I would first like to acknowledge my adviser, Dr. Eric Feigelson, who originated this thesis topic and helped to guide me through the research. I would also like to acknowledge the very helpful input received from Drs. Ethan Schreier, Dan Harris, and Rick Perley. As with almost any scientific research, not excluding my research, there is a large amount of computer work involved. In this light, I would like to thank Ryland Truax, and George Weaver for helping me with some of the more difficlut tasks that I had to do on the computer.

No acknowledgement would be complete without some mention of one's own family. While my family did not provide so much scientific support, the moral support they provided was very important and helped to see me through difficult times. I would especially like to thank my mother, Laura Wood, and my father, Ernest Wood. Together they instilled in me a sense of wonder and curiosity for the world around us.

Chapter I

INTRODUCTION

Purpose

Inverse Compton emission is a basic physical process that involves the interaction of a low frequency photon with a relativistic electron. The electron gives up energy to the photon and consequently a higher frequency photon is created. For ultrarelativistic electrons (Tucker 1975)

$$\nu_f \sim \gamma^2 \nu_i \,, \tag{1}$$

where ν_i and ν_f are the initial and final photon frequencies respectively, and γ is the Lorentz factor. The value of ν_f depends on the incident and scattering angles; and it has a maximum value of $4\gamma^2\nu_i$. Although the initial photons could be any frequency, in extragalactic astronomy one is frequently concerned with the situation where they are the 2.7K microwave background photons ($\nu_i \approx 10^{10}$-10^{11} Hz), and the resultant photons are X-rays ($\nu_f \approx 10^{17}$-10^{18} Hz) when γ is about 10^3 to 10^4.

The radio lobes of galaxies typically have magnetic fields of about 1 to 100 microgauss. When these same regions are emitting synchrotron radiation at radio frequencies (.01 to 100 GHz), then they are a source of ultrarelativistic electrons with a γ of about 10^3 to 10^4. Therefore one might expect to see X-ray lobes of similar shape and extent as the radio lobes. That inverse Compton emission has not been

confirmed is probably due to two factors. A combination of large magnetic fields in the radio lobes, and low photon densities puts the expected inverse Compton flux beyond the limiting sensitivity of available X-ray detectors.

The elliptical galaxy M87 has been shown to have an asymmetric radio halo (Kotanyi 1980; Andernach et al. 1979), with lobes extending several arc minutes to the east and southwest (see Figure 1). Fabricant, Lecar, and Gorenstein (1980) observed M87 in the 0.7-3.0 keV X-ray band using the Imaging Proportional Counter (IPC) of the Einstein Observatory. Their data did not show any asymmetries in the X-ray image. However, using the High Resolution Imager (HRI) on the Einstein Observatory, Schreier, Gorenstein, and Feigelson (1982) discovered asymmetries in the X-ray image of M87 to the east and southwest. The authors found a count excess above background of 0.04 HRI counts/second. Based upon the simple estimates of the magnetic field from radio maps, the expected inverse Compton contribution was about 0.02 HRI counts/second, and therefore was considered a plausible emission mechanism.

M87 is a good candidate for inverse Compton emission for a few reasons. First, the east and southwest asymmetries contained in the radio halo (Kotanyi 1980; Andernach et al. 1979) could be spatially correlated with the X-ray asymmetries found by Schreier, Gorenstein, and Feigelson (1982). Second, the magnetic field in the radio halo is low (about 4 microgauss), and the radio spectrum is steep with $\alpha \simeq 1.2$ (Andernach et al. 1979). The purpose of this research, then, is to use improved radio and X-ray data to: (1) create an X-ray map that shows

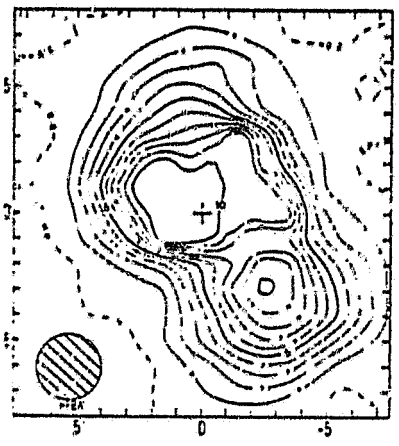

(a)

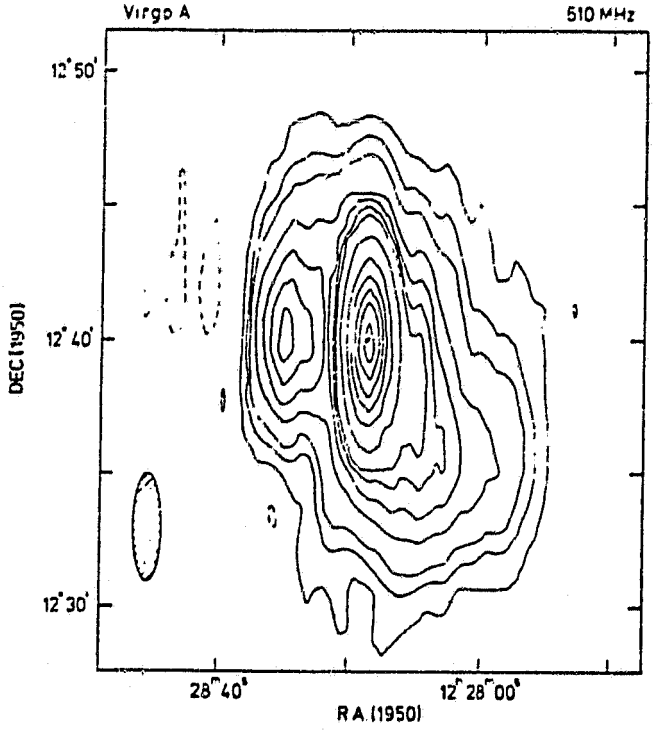

(b)

Figure 1

Radio maps of M87 at 4.8 GHz and 610 MHz. Figure 1(a) is the halo at 4.8 GHz (Andernach et al. 1979). The contour units are .18 Jy/beam. Figure 1(b) is taken at 610 MHz (Kotanyi 1980). The contour levels are 150, 125, 100, 75, 50, 25, 12.5, 10.0, 7.5, 5.0, 2.5, 1.5, 0.5, and -0.5 Jy/beam.

the asymmetric component by removing the symmetric gaseous component; (2) calculate the expected inverse Compton X-ray flux using the radio map and compare to (1); and (3) to determine whether or not the inverse Compton process is occuring. If so, then parameters such as the magnetic field, and the slope and amplitude of the electron energy spectrum (Harris and Grindlay 1979) can be calculated more precisely.

Inverse Compton Effect

Scattering of the 2.7K background can be treated as Thomson scattering since $h\nu' << m_e c^2$, where ν' is the Doppler shifted 2.7K radiation in the rest frame of the electron. The total inverse Compton spectral power per unit volume is (Tucker 1975)

$$j(\nu) = \int P(\nu) N(\gamma) d\gamma \quad \text{ergs cm}^{-3} \text{ sec}^{-1} \text{ Hz}^{-1}, \tag{2}$$

where

$$P(\nu) = 8\pi r_o^2 hc \int f(\nu/4\gamma^2\nu_i) n_{ph}(\nu_i) d\nu_i \tag{3}$$

is the spectral power assuming Thomson scattering with a single electron, $N(\gamma)$ is the electron energy distribution function, ν_i is the initial photon frequency, $n_{ph}(\nu_i)$ is the initial photon number density, and r_o is the classical electron radius. Equation (3) was derived first in the rest frame of the electron and then transformed back to the laboratory frame. The function $f(x)$ is given by

$$f(x) = x + 2x^2 \ln(x) + x^2 - 2x^3 \qquad 0<x<1\,, \tag{4}$$

and represents the Thomson spectrum for a single scattering. The variable x is the ratio of the emitted frequency to the maximum possible frequency $4\gamma^2\nu_i$. For synchrotron emitting radio lobes the electrons follow a power law of the form

$$N(\gamma) = N\gamma^{-n}\,. \tag{5}$$

Equation (2) can then be rewritten

$$j(\nu) = \pi r_o^2 hcN2^{n+3}\left[\frac{n^2+4n+11}{(n+3)^2(n+1)(n+5)}\right] \cdot \nu^{-(n-1)/2}\int_0^\infty \nu_i^{(n-1)/2} n_{ph}(\nu_i)\,d\nu_i\,. \tag{6}$$

The spectral index of the resultant radiation is (n-1)/2. Since the initial photons represent a blackbody, then (Rybicki and Lightman 1979)

$$n_{ph}(\nu_i) = 8\pi\nu_i^2 c^{-3}(e^{h\nu_i/kT} - 1)^{-1} \quad cm^{-3}\,. \tag{7}$$

From equations (7) and (6), and equation 23.2.7 from Abramowitz and Stegun (1970), the final result is

$$\begin{aligned} j(\nu) &= 8(kT)^3 N(r_o \pi/hc)^2 (kT/h\nu)^{(n-1)/2} b(n) \\ &= 4.18\times10^{-40} NT^3 (2.08\times10^{10} T/\nu)^{(n-1)/2} b(n)\,, \end{aligned} \tag{8}$$

where

$$b(n) = 2^{n+3} \frac{n^2+4n+11}{(n+3)^2(n+1)(n+5)} \Gamma\left(\frac{n+5}{2}\right) \xi\left(\frac{n+5}{2}\right). \quad (9)$$

The values of b(n) are tabulated in Table 1. $\xi(x)$ is the Riemann zeta function

$$\xi(x) = \sum_{k=1}^{\infty} k^{-x}. \quad (10)$$

The synchrotron radiation from the relativistic electrons within a radio lobe is given by (Tucker 1975)

$$j(\nu) = 1.70\times10^{-21} N a(n) B^{(n+1)/2} (4.19\times10^{6}/\nu)^{(n-1)/2}, \quad (11)$$

where

$$a(n) = \frac{2^{(n-1)/2}(3/\pi)^{1/2} \Gamma\left(\frac{3n-1}{12}\right) \Gamma\left(\frac{3n+19}{12}\right) \Gamma\left(\frac{n+5}{4}\right)}{8(n+1)\,\Gamma\left(\frac{n+7}{4}\right)}. \quad (12)$$

The values of a(n) are tabulated in Table 1. These values were found to be incorrect (for n>4) in a number of sources, all of which referenced Ginzburg (1964). The calculated values in Table 1 agree with those given by Tucker (1975). Appendix B contains the FORTRAN code used to calculate both a(n) and b(n). Equation (11) assumes the electron distribution to be locally isotropic and follow the power law of equation (5). The electron spectral index, n, is related to the synchrotron spectral index, α, by the relation

Table 1

The functions a(n) and b(n). The error is less than 1×10^{-6}.

n	a(n)	b(n)
0.5	1.3635×10^{0}	3.0064×10^{0}
0.6	8.1296×10^{-1}	3.0039
0.7	5.6718	3.0239
0.8	4.2967	3.0646
0.9	3.4275	3.1253
1.0	2.8341	3.2055
1.1	2.4068	3.3052
1.2	2.0871	3.4247
1.3	1.8405	3.5649
1.4	1.6460	3.7267
1.5	1.4896	3.9115
1.6	1.3620	4.1209
1.7	1.2565	4.3569
1.8	1.1685	4.6218
1.9	1.0944	4.9183
2.0	1.0317	5.2495
2.1	9.7823×10^{-2}	5.6189
2.2	9.3255	6.0306
2.3	8.9341	6.4892
2.4	8.5984	6.9997
2.5	8.3107	7.5682
2.6	8.0646	8.2012
2.7	7.8551	8.9062
2.8	7.6779	9.6919
2.9	7.5297	1.0568×10^{1}
3.0	7.4074	1.1545
3.1	7.3088	1.2635
3.2	7.2319	1.3853
3.3	7.1751	1.5215
3.4	7.1371	1.6737
3.5	7.1167	1.8442
3.6	7.1131	2.0351
3.7	7.1256	2.2492
3.8	7.1535	2.4894
3.9	7.1966	2.7592
4.0	7.2545	3.0623
4.1	7.3271	3.4032
4.2	7.4134	3.7870
4.3	7.5161	4.2194
4.4	7.6326	4.7069
4.5	7.7641	5.2569
4.6	7.9109	5.8781
4.7	8.0734	6.5801
4.8	8.2519	7.3741
4.9	8.4471	8.2728
5.0	8.6596	9.2909

$$n = 2\alpha + 1. \tag{13}$$

From equations (8) and (11) it can be seen that the synchrotron and inverse Compton spectral indices are equal.

For an optically thin source $S_\nu \propto j(\nu)$, where S_ν is the flux density. Therefore

$$S_x/S_r = j(\nu_x)/j(\nu_r)\ , \tag{14}$$

where S_x and S_r are the X-ray and radio flux densities. Using equations (8), (11), and (13) this ratio becomes

$$S_x/S_r = (\nu_r/\nu_x)^{\alpha}\ 2.46\times10^{-19}\, T^{3+\alpha}\, B^{-(\alpha+1)} \cdot (4.96\times10^{3})^{\alpha}\, \frac{b(n)}{a(n)}\ . \tag{15}$$

Because M87 has a low redshift ($z = .004$), corrections for the value of the temperature, T, would be negligible and have not been included.

Morphology of M87

M87 is a giant elliptical (E1) galaxy, and the most massive member of the Virgo cluster. It has an apparent magnitude of about 10, and is 15.7±0.7 Mpc distant (Mould, Aaronson, and Huchra 1980). The ellipticity varies from 0.76 to 3.72 at distances from the nucleus of 40" to 32.5" respectively. An increase in ellipticity such as this is typical for elliptical galaxies. The position angle of the major axis is about 150° and is fairly constant at all distances (Carter and Dixon 1978).

M87 has proven to be an interesting galaxy. The first extragalactic jet ever discovered was observed by Curtis (1918) on the northwest side extending outward from the nucleus about 20". Moreover, M87 is very rich with galactic clusters with current estimates at about 4000 clusters (Harris and Smith 1976). At radio wavelengths, M87 is the third brightest source in the sky. The radio source identifications are Virgo A or 3C274.

M87 was first detected in X-rays by Byram, Chubb, and Friedman (1966) using a rocket borne detector. Subsequent observations (Bradt et al. 1967, Adams et al. 1969, Bowyer et al. 1970, Lampton et al. 1971) confirmed the X-ray detection, however some confusion remained as to whether the X-ray emission was associated with M87 or with the center of the Virgo cluster. Using the Uhuru satellite, Kellogg et al. (1972) found the dominant X-ray emission to be extended by about 1^{o} around, and associated with, M87.

Models for the X-ray emission have been proposed using both thermal (Ginzburg 1967; Malina, Lampton, and Bowyer 1976; Lea et al. 1973) and non-thermal processes (Shklovskii 1967; Brecher and Burbidge 1972). Harris and Romanishin (1974) investigated several clusters of galaxies and found inverse Compton to be a viable mechanism for the generation of of the observed X-rays. It was Turland (1975) who first computed the expected inverse Compton X-ray flux from the radio halo. Using an equipartition magnetic field of 5 microgauss, he found the expected inverse Compton emission to be .02 percent of the total X-ray emission. Because thermal bremsstrahlung predicted the X-ray emission quite well,

Turland (1975) favored it as the emission process. The discovery of iron emission lines (Mushotzky et al. 1978, Lea et al. 1979) and O VIII emission lines (Canizares et al. 1979) confirmed the thermal bremsstrahlung model.

Whereas the early models of the M87 X-ray source were based upon low resolution data; Schreier, Gorenstein, and Feigelson (1982) used the Einstein HRI detector, which has a resolution of 3" full-width at half-maximum (FWHM), to distinguish four regions: (1) a diffuse gas component; (2) a compact nuclear source; (3) an X-ray jet; and (4) an asymmetric component. The diffuse gas component is the large extended region that had been seen by earlier observers using low resolution data, and is the dominant or most luminous feature. The diameter of the nucleus is less than or approximately equal to 3", and may be associated with a central massive object. An accretion efficiency of $< 10^{-4}$ onto a 10^9 $M_\odot$ black hole is required not to exceed the X-ray luminosity of 10^{41} ergs sec^{-1}. The X-ray jet is very well correlated with the well defined jet observed at radio and optical wavelengths. The jet emission at X-ray wavelengths, as well as at longer wavelengths, is due to synchrotron emission. The fourth component, the asymmetric component, is the one of interest for this research. This component is visible in Figure 2 as deviations to the east and southwest from the otherwise spherical, concentric contours of the diffuse gas. The radial distribution of surface brightness is shown in Figure 3 (from Schreier, Gorenstein, and Feigelson 1982). Each set of points represents a 60^o azimuthal bin with vertex at the nucleus. The enhancement in X-rays due to the jet can be seen around 10" from the nucleus in the 240^o to 300^o (plus signs) bin.

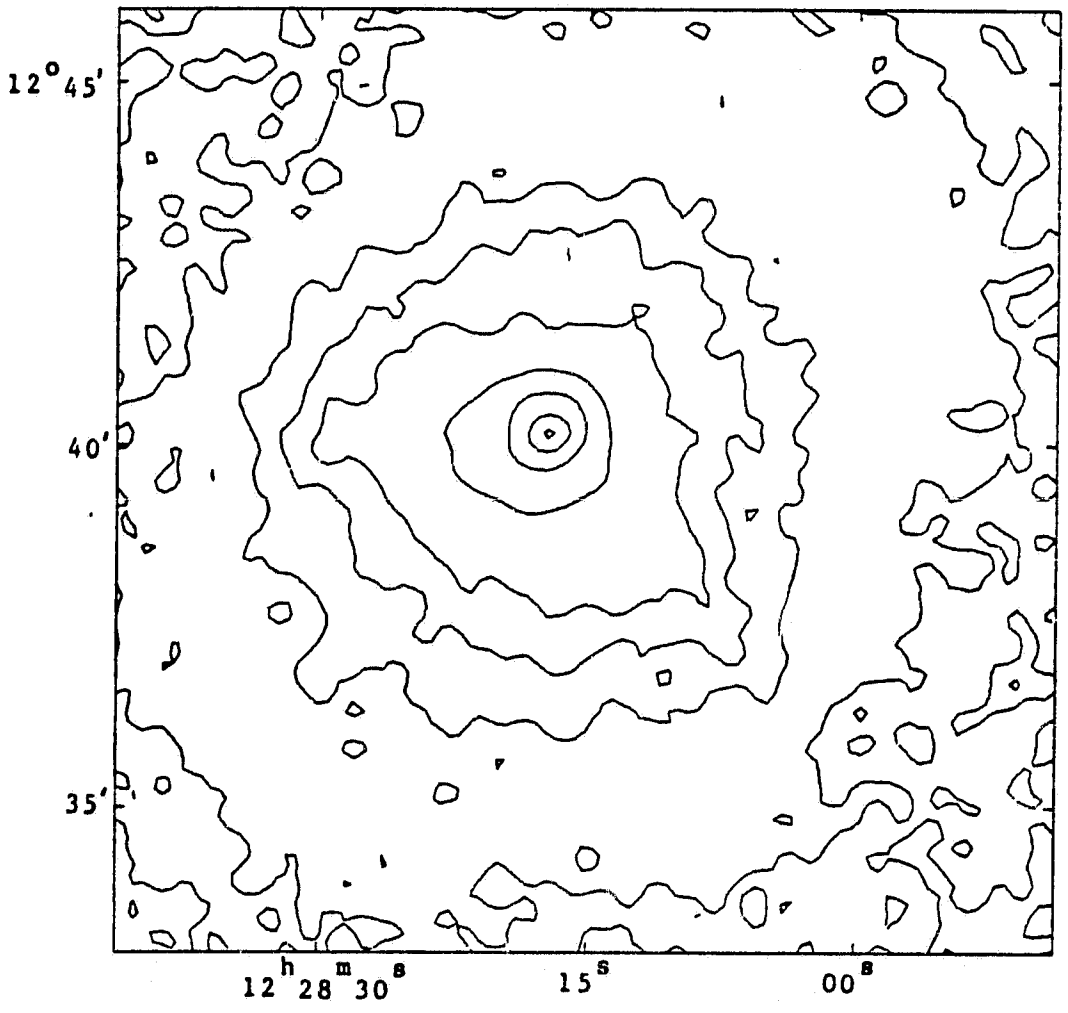

Figure 2

X-ray map of the central 12' Gaussian smoothed with a FWHM of 20". The contour levels are 150, 82, 32.8, 16.4, 8.2, 6.3, 4.9, 3.3, 2.6, 2.1, and 1.3 HRI counts.

The asymmetric component appears as a count excess from about 30" to 5' from the nucleus in the 60^{o} to 120^{o} (filled circles) and 180^{o} to 240^{o} (squares) bins.

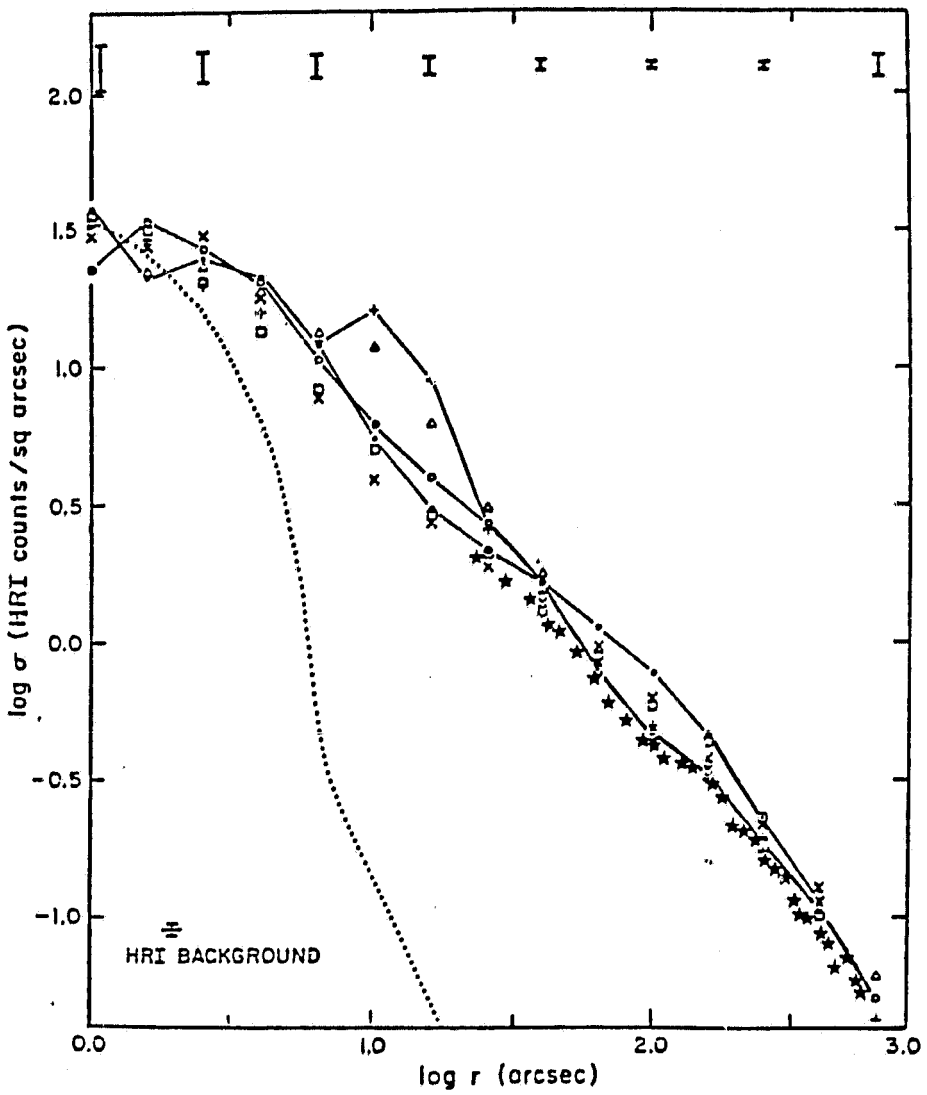

Figure 3

Radial distribution of surface brightness about the nucleus in 60° azimuthal bins. The position angles defining the bins are 0°-60° (open circles), 60°-120° (filled circles), 120°-180° (crosses), 180°-240° (squares), 240°-300° (plus signs), and 300°-360° (triangles). The subtracted instrumental background is shown in the bottom left corner. The error bars at the top are the statistical uncertainties. The HRI point response function is shown by the dotted curve (from Schreier, Gorenstein, and Feigelson 1982). The surface brightness due to the diffuse gas component is plotted using stars.

Chapter II

METHODS

X-ray and Radio Data

The radio and X-ray data for this research were obtained in the form of a Flexible Image Transport System (FITS) tape. The FITS format is described by Wells, Greisen, and Harten (1981).

The HRI was used to collect the X-ray data. The energy band in which the HRI responds is from 0.15 to 1.5 keV. The HRI itself has 4096 by 4096 pixels, each subtending 0.5". The focusing optics of the Einstein telescopes limits the resolution to 3" (Giacconi et al. 1979). The X-ray data was made from two HRI exposures of M87. The first exposure, which was used by Schreier, Gorenstein, and Feigelson (1982), was made on July 5, 1979 and lasted 75,600 seconds. The second exposure was made on December 9, 1980 with a duration of 51,200 seconds. The two images were coaligned and merged together. The data was reprocessed (Rev. 1.0) and only data corresponding to the best satellite aspect solutions (LOCK mode) were kept. The final effective exposure time of the merged image, i.e., the amount of time the instrument was actually collecting data, was 74,464.7 seconds.

The X-ray image stored on the FITS tape was a 512 by 512 matrix of 4" by 4" pixels. Rather than using the entire image, a 315 by 315 subset array contered on the nucleus was kept. This was done for two reasons. First, the subset array contains roughly one third the number of pixels in the full array. Therefore much less disk space was required

for storage; and the computation times were greatly decreased. Second, the subset array extends 10' from the nucleus. This is ample space since the radio lobes extend outward about 5'. Figure 2 is a contour plot of the central 12' of the X-ray data smoothed with a Gaussian function with a FWHM of 20".

The radio data was collected from the National Radio Astronomy Observatory's (NRAO) Very Large Array (VLA), and represents the sum of two data sets. The first data set is a D configuration snapshot made by R. Perley in October 1981. The second data set is a hybrid C/A configuration synthesis obtained by E. Feigelson, E. Schreier, and D. Harris. For this configuration the telescopes on the north arm were more widely spaced than those on the east and west arms. Both data sets were observed at a wavelength of 20 cm (1452.4 MHz). The self calibration at high resolution of the second data set was not perfect. The data set contains a few residual stripes which show up as narrow linear contours. The wide spacing on the north arm and the related lack of north-south baselines, as well as the large dynamic range of radio intensities across the galaxy (roughly 1000 to 1 from the nucleus to the halo), are possible causes of the self-calibration difficulty. Despite these difficluties, the radio halo structure appears reliable.

The radio data on the FITS tape was a 512 by 512 pixel array (each pixel was 4" on a side). Similar to the X-ray data, a 315 by 315 subset array centered on the nucleus was kept. Figure 4 is a contour plot of the central 12' of the data.

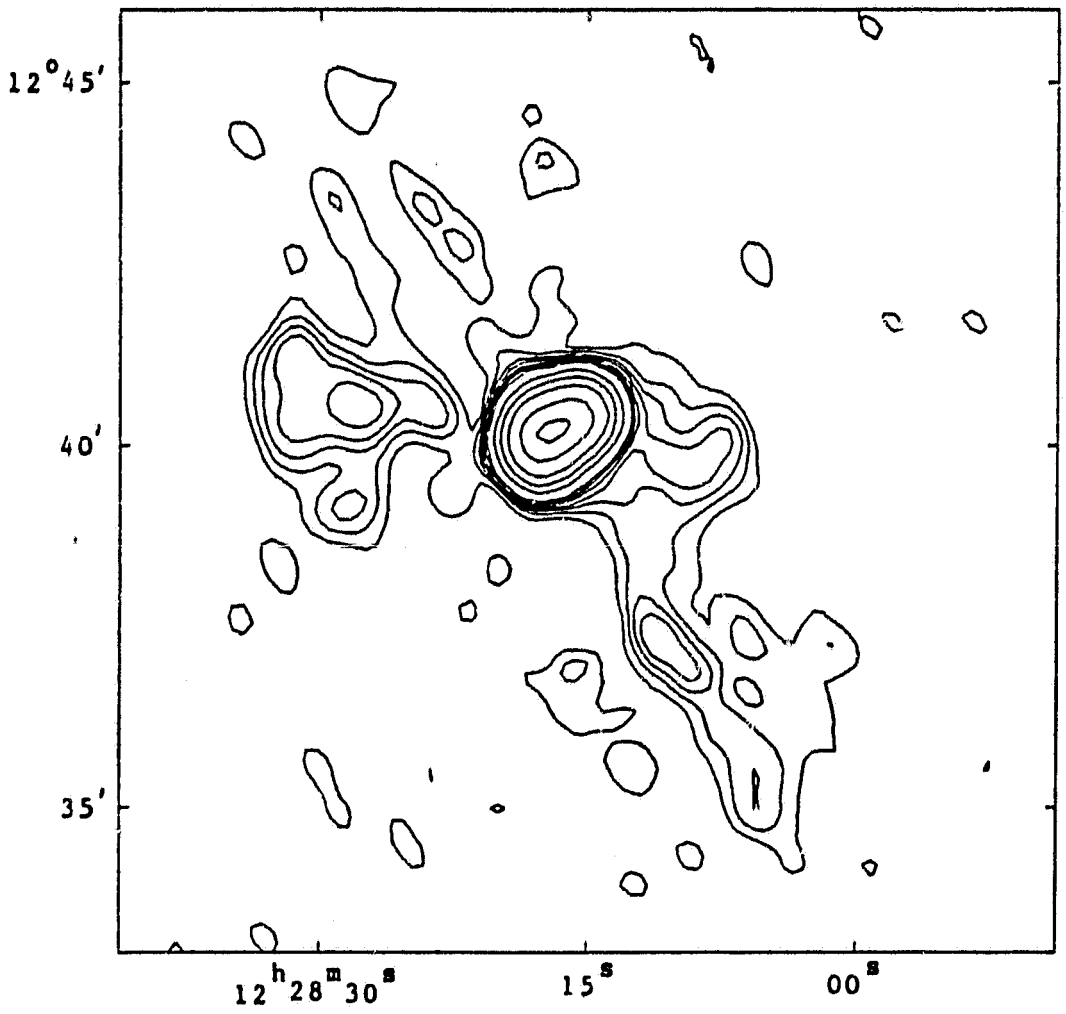

Figure 4

Radio map of the central 12'. The observation frequency was 1.4524 GHz. The contour levels are 54.88, 30.50, 12.20, 6.10, 3.05, 1.22, 0.98, 0.79, 0.61, 0.49, 0.37, 0.24, and -0.24 Jy/beam.

Subtraction of the Diffuse Gas Component

In order to calculate the X-ray contribution from the asymmetric component, it was necessary to separate this component from the other three components. The compact nuclear source is approximately 3" in size or a little less than one pixel (4"). The X-ray jet extends for about 20" or five pixels. Since the X-ray map is nearly centered on the nucleus (within 4" of the middle pixel), then ignoring the center pixels (out to a radius of five pixels) would be the simplest adequate way to remove the jet and nucleus.

The diffuse gas component and the asymmetric component are not as easily separated because everywhere the asymmetric component occurs the diffuse gas component is also present. A simplification is possible if the diffuse gas is assumed to be spherically symmetric about the nucleus. From Figure 3 it can be seen that the slope of the different curves is approximately -1. Since it is a log-log plot, then a negative slope implies that the count density (HRI counts/square arcsecond) is inversely proportional to the distance from the nucleus. Therefore the slope of the count density would be very steep close to the nucleus, and far away the slope would be near zero. The diffuse gas component can, with the two assumptions above, be removed without need of any physical models for the type of emission involved. To do this, the X-ray map was divided into azimuthal pie slices and differentially spaced concentric circles, where two consecutive circles enclose an annulus (for example, the first and second circles define the first annulus). The first circle had a radius of five pixels, therefore excluding the nucleus and jet

from any bin. The basic idea is to make the bins small enough to accurately sample the radial and azimuthal variations. Because azimuthal variations occur over large angles, a pie slice of 45^{o} was adequate. Since this creates eight pie slices, they are hereafter referred to as octants. The circles were spaced according to the formula

$$\Delta_{N+1} = N/R_F \, , \tag{16}$$

where R_F is a constant, N is the circle number, and Δ_{N+1} is the increase in radius (which is the same as the spacing between circles) of the $(N+1)^{th}$ circle. The minimum value that Δ_{N+1} could be was set to 1.5 pixels. The value of R_F was chosen so that the spacing between circles was small enough to accurately sample the steep gradient of the count density near the center, while at the same time avoiding needless oversampling further away where the gradient was small. Figure 5 shows the final binning of the X-ray map for R_F = 4 pixels (16").

Each annulus contains eight bins defined by the boundaries of the octants. The count density (here referring to HRI counts per pixel) was computed for each bin. Under the assumption that the diffuse gas component is spherically symmetric, the minimum count density within each annulus would represent that component without enhancement from the asymmetric component. Therefore, each annulus was assigned the lowest count density contained within it. Because each annulus was wider than one pixel, the minimum count density had to be associated with some specific radial distance. This distance was chosen to be the point that bisects the area of the annulus. Two arrays were, therefore, created;

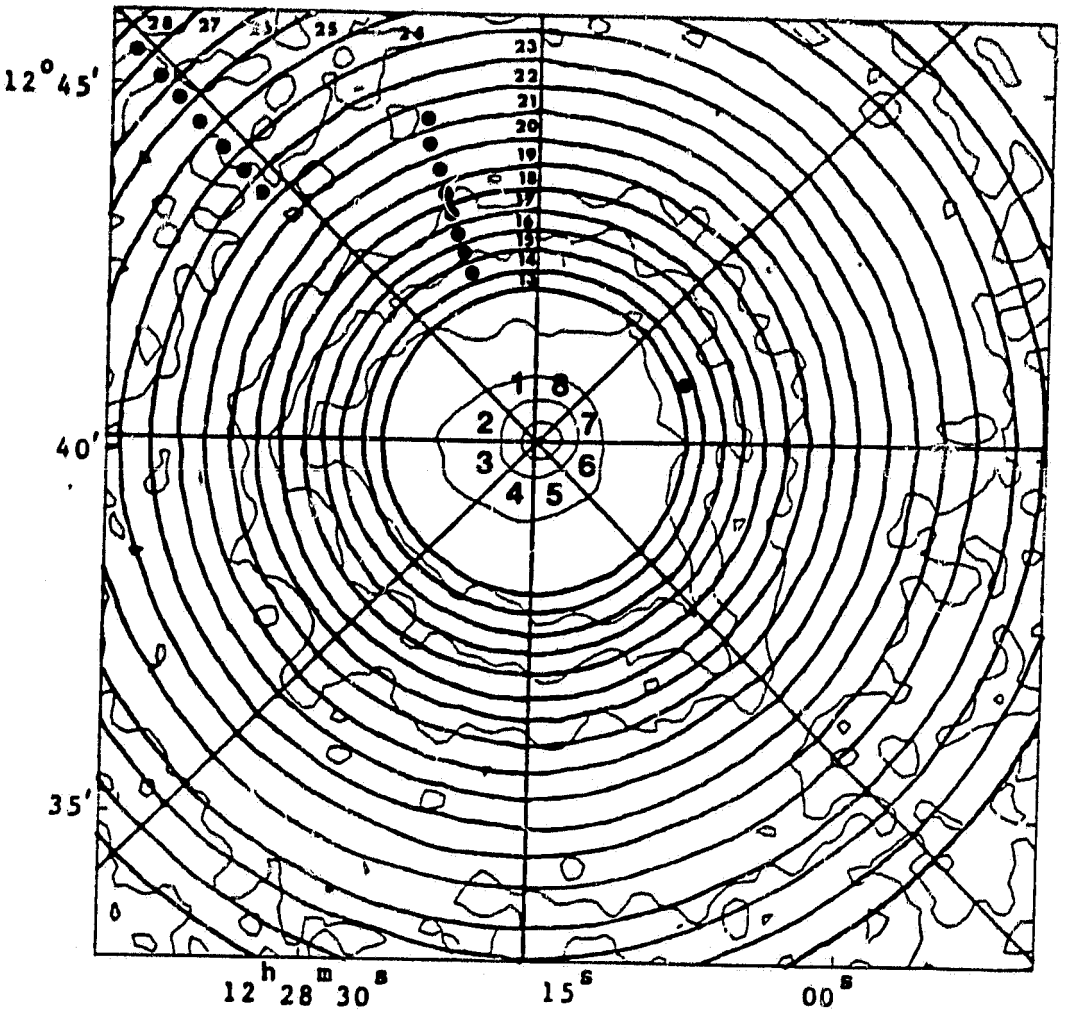

Figure 5

Radial and azimuthal binning of the X-ray map. Annuli 1 through 12 have been left out for clarity. The filled circles indicate which bin had the lowest count density within that annulus. The underlying contour plot is the same as Figure 2.

one contained radial distances, and the second contained the minimum count densities associated with the radial distances. The minimum count densities are plotted on Figure 3 with stars. The points follow the lower edge of the data from Schreier, Gorenstein, and Feigelson (1982), which is the expected result if they are to represent the diffuse gas component. Therefore, using these points, and quadratic interpolation for intermediate pixels, the diffuse gas component can be subtracted from the X-ray image. The subtraction then leaves only the asymmetric component, which is shown in Figure 6. The FORTRAN program XSUB VSFOR (see Appendix A) performs the subtraction described above. It contains the variable ROTATE which rotates the pie slices from their zero position shown in Figure 5. To test the constancy of the subtraction, the pie slices were rotated 20^{o} counter-clockwise. The subtracted data was found to deviate negligibly from the unrotated results. Therefore, the subtraction was invariant under this rotation.

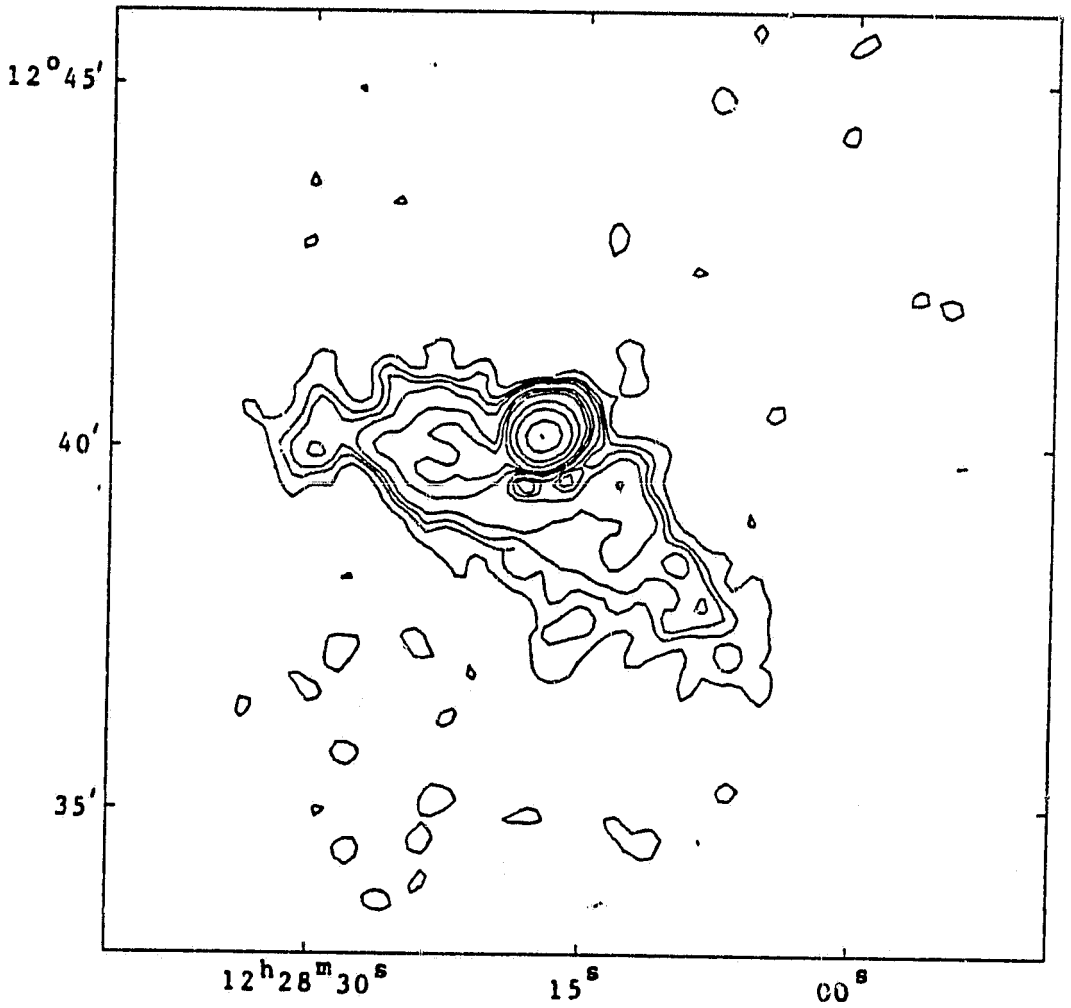

Figure 6

X-ray map of the asymmetric component Gaussian smoothed with a FWHM of 20". The contour levels are 150, 82, 32.8, 16.4, 8.2, 6.3, 4.9, 3.3, 2.6, 2.1, 1.3, and -0.6 HRI counts.

Chapter III

RESULTS

The Radio Map

The VLA data, used to create the radio map shown in Figure 4, is not as good as the X-ray data from the HRI. Despite this, there are a few features that are probably reliable. The most prominent feature is the asymmetry in the radio halo. There is a distinct east lobe extending about 4.5' from the nucleus, and a southwest lobe extending about 7' from the nucleus. These two lobes are seen in the data of Andernach et al. (1979) and the 610 MHz data of Kotanyi (1980). Their data is shown in Figure 1. There is also a smaller lobe extending 2' west of the nucleus, and directly opposite the east lobe. The smaller west lobe has approximately the same surface brightness as the larger east and southwest lobes. This feature does not show up in the data of Kotanyi (1980), but is somewhat visible in 4.8 GHz map of Andernach et al. (1979). A later 1465 MHz map by R. Perley is shown in Figure 7. This is a moderate resolution map (FWHM=62") which shows all of the features above as well as an elliptically shaped halo with a major axis about 15' long and elongated northeast to southwest. The southwest lobe is enveloped by the halo, whereas the east and west lobes appear distinct from it.

The X-ray Map

The asymmetric X-ray component shown in Figure 6 contains several interesting features. There are two lobes present. One lobe extends

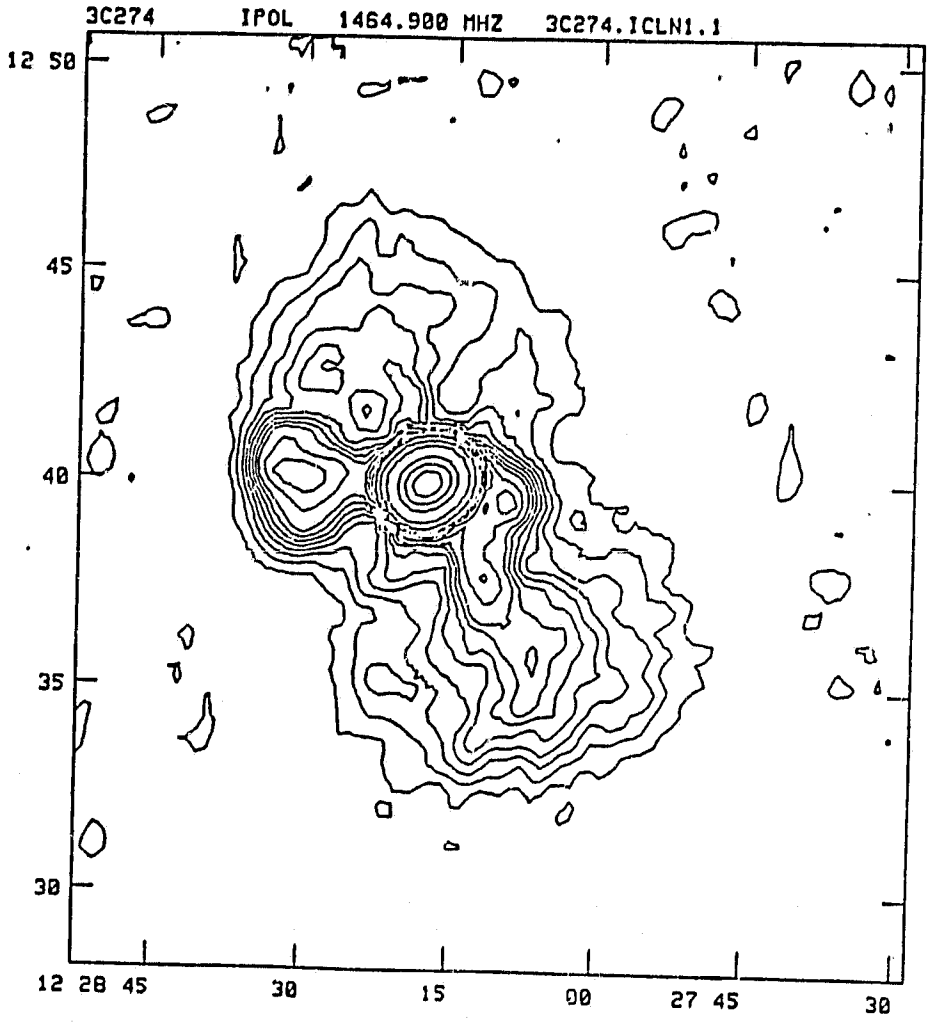

Figure 7

Radio map of M87 at 1.465 Ghz (Perley 1983). The contour levels are 67.6, 45.0, 27.0, 9.0, 4.5, 2.7, 2.4, 2.2, 1.9, 1.6, 1.4, 1.1, 0.90, 0.81, 0.72, 0.54, 0.36, 0.27, 0.18, and -0.18 Jy/beam.

about 4' east from the nucleus, and has a FWHM of about 1' at a distance of 1' from the nucleus. The other lobe extends about 5' southwest from the nucleus. The FWHM of this lobe is about 0.7' at a distance of about 2.5' from the nucleus. These lobes do not seem to extend any further than this, even at low surface brightness. This was indicated by the relatively steep gradient off the ends of the lobes on a more smoothed map. There is a "bridge" of emission extending about 2' south and southeast of the nucleus which connects the east and southwest lobes. Another feature seen is a large diffuse X-ray emitting region. It shows up as a sprinkling of low-level contours in the northwest and southeast quadrants, and extends about 15' from the northwest corner to the southeast corner. This large diffuse region could be the X-ray gas counterpart of the optical ellipticity. The position angle of the major axis is equivalent to that found by Carter and Dixon (1978) at optical frequencies. Figure 8 shows the above mentioned regions. Regions 1 and 3 are the east and southwest lobes, respectively. Region 2 is the "bridge" of emission; and regions 4 and 5 together are the large diffuse region.

In order to compare the X-ray asymmetric component and radio maps quantitatively, a conversion factor from HRI counts to Janskys is required. The values of N_H and α (the spectral index for the X-ray emission) need to be determined. From Stewart et al. (1984), the N_H contribution (assuming model C) from M87 was estimated to be 10^{21} cm^{-2}. However, the gas temperature is approximately 2×10^7K which would completely ionize elements up to about argon. Therefore the N_H contribution from M87 would be negligible. From our galaxy N_H is generally

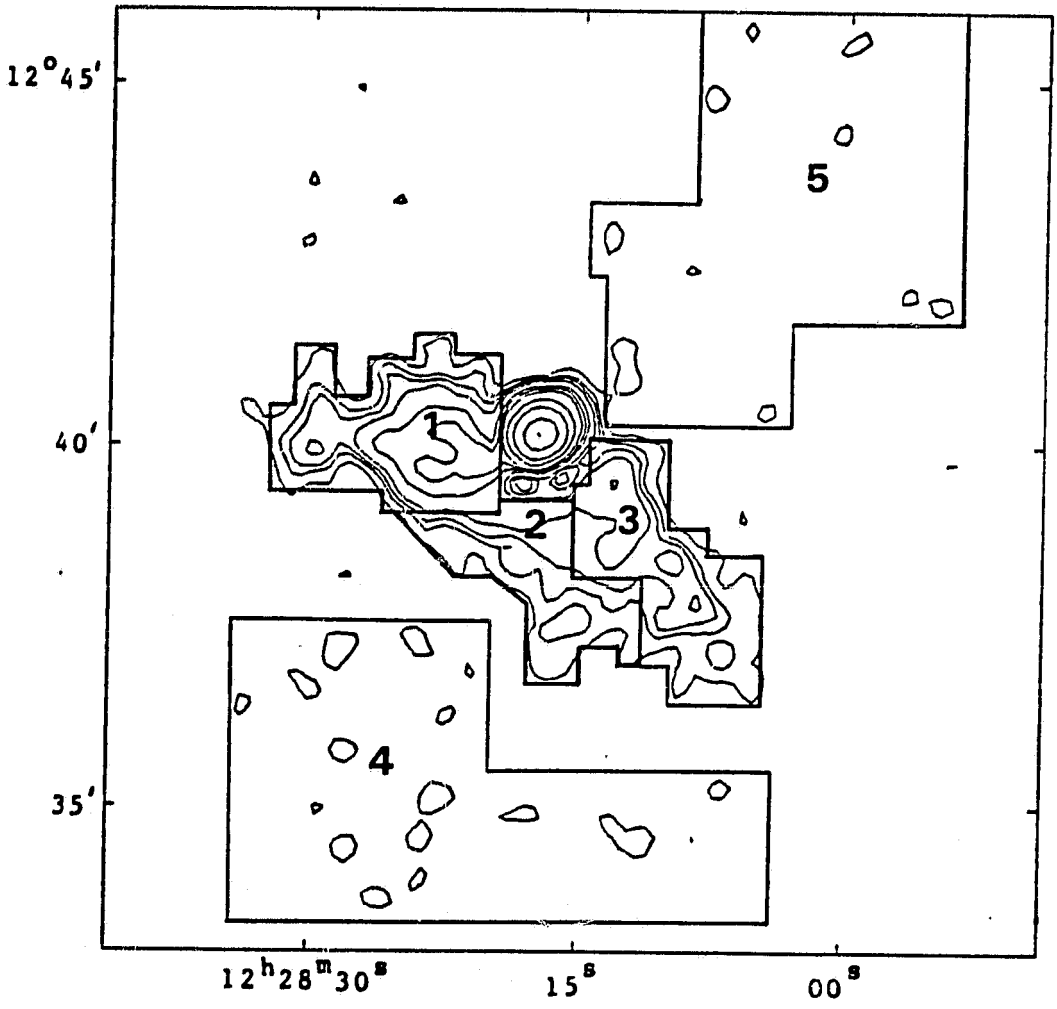

Figure 8

X-ray map of the asymmetric component separated into five regions. The underlying contour plot is from Figure 6.

accepted to be about 4×10^{20} cm^{-2}, and so this was the value used. The spectral index for inverse Compton radiation is equal to the spectral index for the synchrotron radiation of the relativistic electrons that are scattering the photons. Using the halo flux values at different radio frequencies from Andernach et al. (1979), α was found to be about 1.2.

The following equations convert HRI counts to flux and flux density,

$$NET/1000 = CTS * DTC * 1000 / EXP, \quad (17)$$

$$F = CF_F * 0.8 * 0.7924 * NET/1000, \quad (18)$$

$$S = CF_S * 0.8 * 0.7924 * NET/1000, \quad (19)$$

where CTS is the total HRI counts, DTC is the dead time correction, EXP is the exposure time, CF_F is the flux conversion factor, and CF_S is the flux density conversion factor. The conversion factors (for the given N_H and α) from the Einstein Observatory User's Manual are, $CF_F = 1.47 \times 10^{-13}$ in the 0.2 to 4 KeV band, and $CF_S = 1.61 \times 10^{-31}$ at 1 KeV. Table 2 gives the flux and flux densities for the five regions of Figure 8. The values given in Table 2 contain errors from a few different sources. One source of error is from the photon counting statistics. Because

Table 2

X-ray fluxes and luminosities for the five regions of Figure 8. The area is in arcmin^2; F_X is in ergs cm^{-2} sec^{-1}; L_X is in ergs sec^{-1}; and S_X is in ergs cm^{-2} sec^{-1} Hz^{-1}.

Region	Area	F_X(0.2-4 KeV)	L_X(0.2-4 KeV)	S_X(1 KeV)
1	6.12	5.7×10^{-12}	1.7×10^{41}	6.2×10^{-30}
2	4.26	2.5×10^{-12}	7.3×10^{40}	2.7×10^{-30}
3	5.88	3.8×10^{-12}	1.1×10^{41}	4.2×10^{-30}
4	23.4	4.9×10^{-12}	1.5×10^{41}	5.4×10^{-30}
5	23.0	4.0×10^{-12}	1.2×10^{41}	4.4×10^{-30}

there are so many counts (on the order of a few thousand), a range of $\pm 1\sigma$ represents less than ±2 percent of the total counts. This error is negligible compared to the other errors. An important source of error is in the conversion factors CF_F and CF_S. Given the uncertainties in α and N_H, the conversion factors can vary by as much as a factor of two. In addition to this, the luminosity depends on the distance to M87, and the value for this varies from 15.7±0.7 Mpc (Mould, Aaronson, and Huchra 1980) to 21.9±0.8 Mpc (Sandage, and Tammann 1976).

Equation 15 relates the X-ray radio flux densities. It was modified to use more familiar units. Putting in T = 2.7K and converting the units, the result is

$$S_x/S_r = (\nu_r/E_x)^{\alpha} 4.84\times10^{-41} B^{-(\alpha+1)} (5.54\times10^{-5})^{\alpha} \frac{b(n)}{a(n)}, \quad (20)$$

where S_x is in ergs cm^{-2} sec^{-1} Hz^{-1}, S_r is in Janskys, ν_r is in GHz, E_x is in KeV, and B is in gauss.

Chapter IV

DISCUSSION

The results so far indicate that M87 contains an asymmetric radio halo which, because of the high surface brightness, is generally accepted to be emitting via synchrotron radiation. The X-ray image also contains an asymmetric component which is similar in size and shape to the radio halo. The emission mechanism for the X-rays could be linked to the ultrarelativistic electrons in the radio halo with an inverse Compton model. Alternatively, the X-ray emission could be due to a background cluster.

X-ray Cluster Emission

Huchra and Brodie (1984) observed five galaxies that were within a few arcminutes of M87. Because their velocities are 25 times that of M87 indicates that they are background galaxies. The radial velocity distribution is about 300 km sec^{-1} which indicates that they could be members of a poor cluster. The calculated distance to this possible cluster, using H_0 = 75 km sec^{-1} Mpc^{-1}, is about 343 Mpc. The positions of these galaxies with respect to M87 are shown in Figure 9. Two of the brighter galaxies, 87-1063 and 87-1169 (3 and 5 respectively on Figure 9), coincide well with the southwest lobe. The other three appear to have no obvious connection with the asymmetric component.

Huchra and Brodie (1984) suggest that the hypothesis of Schreier, Gorenstein, and Feigelson (1982) that inverse Compton emission is

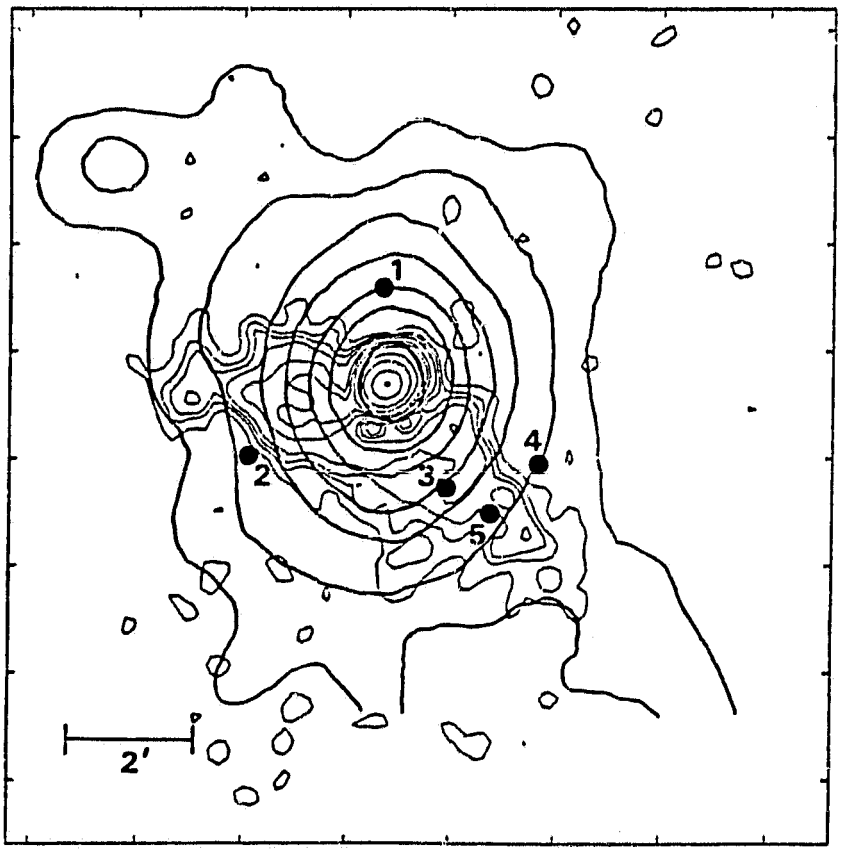

Figure 9

Positions of the five background galaxies. Galaxy 87-869 is 1, 87-522 is 2, 87-1063 is 3, 87-1303 is 4, and 87-1169 is 5. The thin contours are the asymmetric component (see Figure 6). The bold contours represent the poor cluster AWM 4 if it were behind M87 and 343 Mpc away.

occuring in the halo requires reexamination in light of the discovery of this background cluster. In order to do this, an estimate of the cluster X-ray emission is required. Kriss, Cioffi, and Canizares (1983) made X-ray observations of 16 poor clusters. Unfortunately, the X-ray luminosity varied from $< 1.07 \times 10^{42}$ to 1.02×10^{44} ergs sec^{-1}, and so could not be used reliably. From the flux values for regions 1, 2, and 3 (see Table 2), the expected X-ray luminosity for the asymmetric component, if M87 were 343 Mpc away, is 1.7×10^{44} ergs sec^{-1}. This is about 150 times brighter than the least luminous cluster, and about 1.5 times brighter than the most luminous cluster. A convincing argument can be based on the shape of the asymmetric component. A "typical" X-ray cluster has a more or less spherical symmetry. The bold contours on Figure 9 are the X-ray map of a typical poor cluster, AWM 4, positioned as if it were directly behind M87 and 343 Mpc away, which is the distance of the poor cluster discovered by Huchra and Brodie (1984). The figure shows that while the asymmetric component of M87 has about the right angular size, it is highly improbable that a background cluster would have such a unique shape and be centered around the nucleus of M87. From the above arguments it would be unlikely that the background cluster is contributing significantly to the observed X-ray asymmetry.

The background cluster can also be shown to be unable to account for the halo emission at radio frequencies. Owen (1974) catalogued several hundred Abell clusters. Those clusters with a richness class R=0, and a distance class D=4, were used to obtain an average cluster flux density at 1400 MHz of 0.56±0.07 Janskys. This is negligible compared to the M87 radio halo flux of 80 Janskys at 1420 MHz. Therefore,

at radio wavelengths the background poor cluster could not be the source of the observed asymmetry.

Inverse Compton Emission

Because the radio data has a lower resolution than the X-ray data, the two maps could not be easily compared quantitatively using equation 20. Qualitatively some interesting comparisons can be made. Figure 10 shows the radio halo and X-ray asymmetric component maps plotted with the same scales. Both maps have major lobes to the east and southwest. The two east lobes have similar postion angles of about 85^{o}. However the southwest lobe on the X-ray map has a position angle of 225^{o}, while the southwest lobe on the radio map has a position angle of approximately 210^{o}. The small west lobe on the radio map appears to have no corresponding feature on the X-ray map. Similarly, the "bridge" between the X-ray east and southwest lobes does not appear on the radio map.

The halo flux density could not be be accurately found from the radio data. The larger spatial features were not contained in the original VLA database used to make the radio map shown in Figure 4. The result is that the data does not contain enough information to calculate the radio halo flux density. Therefore, to quantitatively check for inverse Compton emission, the radio halo flux densities of Andernach et al. (1979) were used. An equipartition magnetic field of 4 microgauss in the halo was assumed. This corresponds to a minimum energy for the relativistic particles and the magnetic field of about 10^{58} ergs. The relativistic particles are assumed to be entirely electrons (Andernach et al. 1979). The X-ray flux density used was the sum of the flux den-

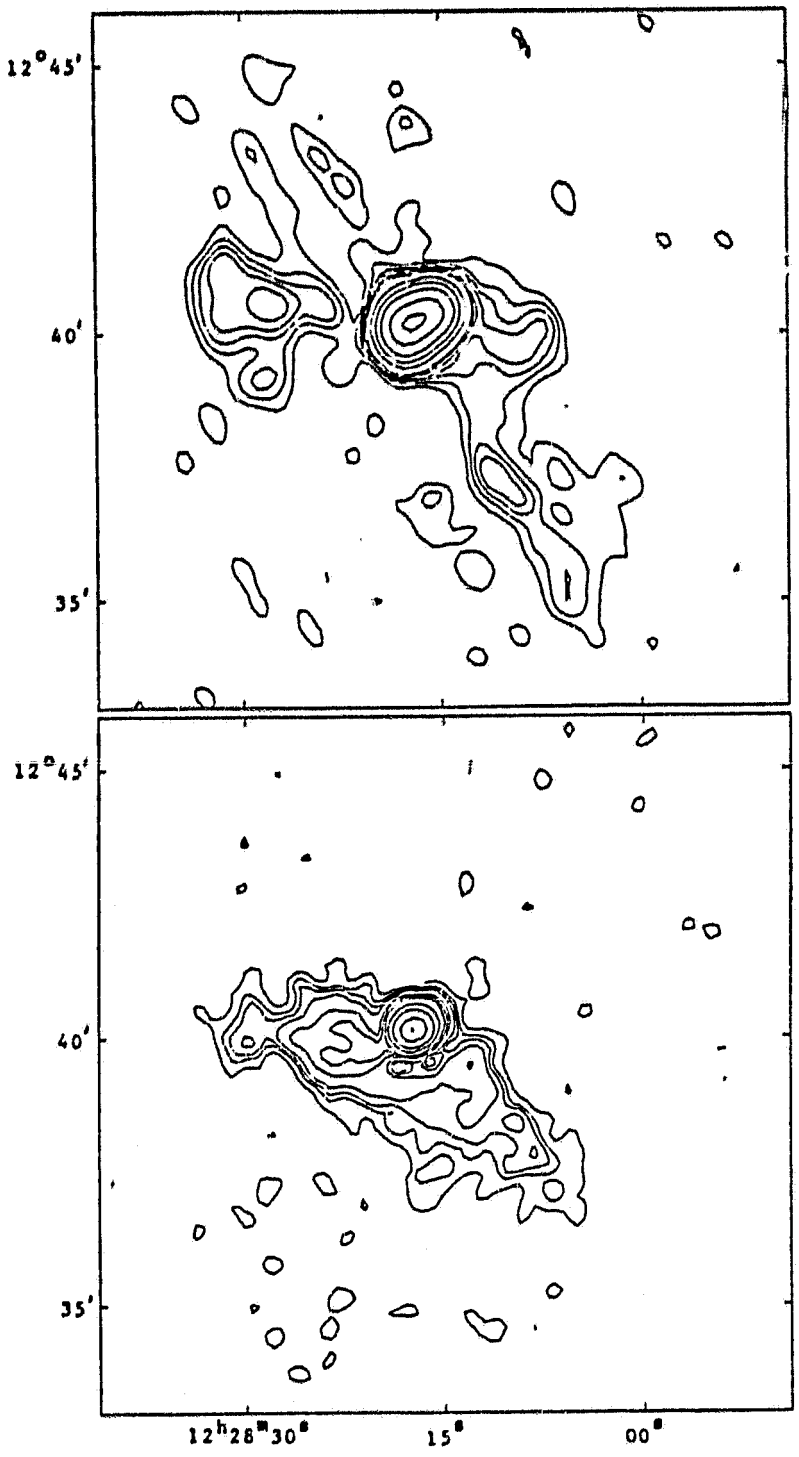

Figure 10

Radio halo and X-ray asymmetric component. Figure 10(a) is the same as Figure 4. Figure 10(b) is the same as Figure 6. The scales for both maps are the same.

sities from regions 1, 2, and 3 from Table 2. Therefore, using $S_X = 1.3 \times 10^{-29}$ ergs cm^{-2} sec^{-1} Hz^{-1}, $E_X = 1$ KeV, $B = 4 \times 10^{-6}$ gauss, $\nu_r = 1.420$ GHz, and $\alpha = 1.2$, the expected radio flux density from equation 20 is 128 Janskys. This is about 50 percent higher than the value of 80 Janskys given by Andernach et al. (1979).

The calculation above involves considerable uncertainties, not the least of which is the magnetic field orientation. Equation 20 is the average over all angles. Dennison (1980) provides a very thorough analysis of the problem of inverse Compton emission. He estimates the magnetic field in the halo to be about 1-5 microgauss, with the most probable value being about 2.5 microgauss. The expected inverse Compton contribution to the total X-ray luminosity in the 2-6 KeV band then is a little less than 1 percent. The total X-ray luminosity is about 6.2×10^{42} ergs sec^{-1} (0.2-4 KeV). The asymmetric component (regions 1, 2, and 3 from Table 2) has a luminosity of about 3.6×10^{41} ergs sec^{-1} (0.2-4 KeV). Therefore these measurements indicate that inverse Compton accounts for about 6 percent of the total X-ray luminosity.

Summary

None of the data discussed so far provides conclusive proof for inverse Compton emission. However, calculated values are close enough to observed values that it is a very plausible mechanism. One important difficulty is that the percentage of inverse Compton luminosity contained in the total X-ray luminosity can vary from about 0.1 percent to more than 70 percent (Dennison 1980). The amount of the variation depends on the model, i.e., whether the X-ray emitting diffuse gas com-

ponent is isothermal or power law. There is also a strong dependence on the orientation of the magnetic field in the halo. A power law is the favored model for the diffuse gas (Stewart et al. 1984), and is consistent with inverse Compton contributing 6 percent of the total X-ray luminosity (see Figure 3, Dennison 1980). Therefore the inverse Compton intensity as seen by a particular observer can literally be turned on or off from region to region depending upon the orientation of the magnetic field, and the amount of random magnetic field that is present. This could, for instance, account for the spatial dissimilarities between the X-ray and radio map. These are not trivial problems to deal with. Their solution would appear to lie with better, higher resolution, radio data. Also polarization vectors for the radio halo would help to determine the direction of the magnetic field.

At the upper limit, the X-ray cluster mentioned in a previous section could account for about 60 percent of the X-ray luminosity coming from the asymmetric component. This means that the cluster could be providing 4 percent of the total X-ray luminosity, and inverse Compton the remaining 2 percent. A 2 percent inverse Compton contribution is perhaps even more consistent with the consideratins brought out by Dennison (1980). However, the unique shape of the asymmetric component would seem to preclude the X-ray cluster as a possibility. The cluster could have a luminosity closer to the lower limit, in which case the contribution would be insignificant.

Region 2 (see Figure 8) is an interesting region. There is no corresponding radio feature visible on Figure 4. However, there is weak

radio emission from that region as can be seen on Figure 7. Region 2 could be due to the background cluster, or a different emission process from inverse Compton. It is also possible that the X-ray emitting diffuse gas is centered southeast of the nucleus.

In conclusion, the results of this work have reinforced the hypothesis of inverse Compton emission from the radio halo. They are consistent with the radio data of Andernach et al. (1979), but the inverse Compton X-ray luminosity is a little high according to Dennison (1980). The radio and X-ray asymmetric component maps show strong similarities, and the differences could be explainable as due to a change in the magnetic field's direction.

BIBLIOGRAPHY

Abramowitz, M., and Stegun, I. A. 1970, Handbook of Mathematical Functions, (New York: Dover).

Adams, D. J., Cooke, B. A., Evans, K., and Pounds, K. A. 1969, Nature, 222, 757.

Andernach, H., Baker, J. R., von Kap-herr, A., and Wielebinski, R. 1979, Astron. Astrophys., 74, 93.

Bowyer, C. S., Lampton, M., Mack, J., and De Mendonca, F. 1970, Astrophysical Journ., 161, L1.

Bradt, H., Mayer, W., Naranan, S., Rappaport, S., and Spada, G. 1967, Astrophysical Journ., 150, L199.

Brecher, K., and Burbidge, G. R. 1972, Nature, 237, 440.

Byram, E. T., Chubb, T. A., and Friedman, H. 1966, Science, 152, 66.

Canizares, C. R., Clark, G. W., Markert, T. H., Berg, C., Smedira, M., Bardas, D., Schnopper, H., and Kalata, K. 1979, Astrophysical Journ., 234, L33.

Carter, D., and Dixon, K. L. 1978, Astron. Journ., 83, 574.

Curtis, H. D. 1918, Pub. Lick Observatory, 13, 11.

Dennison, B. 1980, Astrophysical Journ., 236, 761.

Fabricant, D., Lecar, M., and Gorenstein, P. 1980, Astrophysical Journ., 241, 552.

Giacconi, R., et al. 1979, Astrophysical Journ., 230, 540.

Ginzburg, V. L. 1967, Soviet Astron., 10, 719.

Ginzburg, V. L., and Syrovatskii, S. I. 1964, The Origin of Cosmic Rays, (New York: The Macmillan Company).

Gorenstein, P., Fabricant, D., Topka, K., Tucker, W., and Harnden, Jr., F. R. 1977, Astrophysical Journ., 216, L95.

Harris, D. E., and Grindlay, J. E. 1979, Monthly Notices Royal Astronomical Soc., 188, 25.

Harris, D. E., and Romanishin, W. 1974, Astrophysical Journ., 188, 209.

Harris, W. E., and Smith, M. G. 1976, Astrophysical Journ., 207, 1036.

Huchra, J., and Brodie, J. 1984, Astrophysical Journ., 280, 547.

Kellogg, E., Gursky, H., Tananbaum, H., and Giacconi, R. 1972, Astrophysical Journ., 174, L65.

Kotanyi, C. 1980, Astron. Astrophys., 83, 245.

Kriss, G. A., Cioffi, D. F., and Canizares, C. R. 1983, Astrophysical Journ., 272, 439.

Lampton, M., Bowyer, S., Mack, J. E., and Margon, B. 1971, Astrophysical Journ., 168, L1.

Lea, S. M., Mason, K. O., Reichert, G., Charles, P. A., and Riegler, G. 1979, Astrophysical Journ., 227, L67.

Lea, S. M., Silk, J., Kellogg, E., and Murray, S. 1973, Astrophysical Journ., 184, L105.

Malina, R., Lampton, M., and Bowyer, S. 1976, Astrophysical Journ., 209, 678.

Mould, J., Aaronson, M., and Huchra, J. 1980, Astrophysical Journ., 238, 458.

Mushotzky, R. F., Serlemitsos, P. J., Smith, B. W., Boldt, E. A., and Holt, S. S. 1978, Astrophysical Journ., 225, 21.

Owen, F. N. 1974, Astron. Journ., 79, 427.

Rybicki, G. B., and Lightman, A. P. 1979, Radiative Processes in Astrophysics, (New York: John Wiley & Sons).

Sandage, A., and Tammann, G. A. 1976, Astrophysical Journ., 210, 7.

Schreier, E. J., Gorenstein, P., and Feigelson, E. D. 1982, Astrophysical Journ., 261, 42.

Shklovskii, I. S. 1967, Soviet Astron., 11, 45.

Stewart, G. C., Canizares, C. R., Fabian, A. C., and Nulsen, P. E. J. 1984, Astrophysical Journ., 278, 536.

Tucker, W. H. 1975, Radiation Processes in Astrophysics, (Cambridge, Massachusetts: MIT Press).

Turland, B. D. 1975, Monthly Notices Royal Astronomical Soc., 170, 281.

Wells, D. C., Greisen, E. W., and Harten, R. H. 1981, Astron. Astrophys., 44, 363.

APPENDIX A

FORTRAN Program to Subtract the Diffuse Gas Component

```
//V01XXXXX JOB
// EXEC FVCG,PARM='OPTIMIZE(1)'
//SOURCE.SYSIN DD *
C*************************************************************************
C PROGRAM: XSUB VSFOR
C
C PURPOSE: To subtract the symmetrical (i.e., hot gas) component from
C          the HRI X-ray image of M-87.
C
C LOCAL VARIABLES:
C   ANN() ....... Annuli boundaries
C   CTS() ....... Counts within a given annulus and pie slice
C   DATA() ...... Array to hold the data
C   DELPHI ...... Size of pie slices in degrees
C   DENMIN() .... Minimum count density for a pie slice in an annulus
C   FILIN ....... Input file name
C   FILOUT ...... Output file name
C   IDATA() ..... Array to hold position information
C   IYCEN,IXCEN . Center of symmetric component subtraction
C   JPHI ........ Index number for pie slices
C   LBOX() ...... Number of pixels within a given annulus
C   MAXANN ...... Number of annuli
C   MAXREG ...... Number of regions bounded by annuli
C   NBOX() ...... Number of pixels within a given annulus and pie slice
C   NPHI ........ Number of pie slices
C   NROWS,NCOLS . Number of rows and columns in the data
C   PHIMIN() .... Pie slice containing DENMIN()
C   PNAME ....... Program name
C   R() ......... The radius to point between annuli bisecting the area
C   RADDEG ...... Factor to convert radians to degrees
C   RADMAX ...... Maximum distance from IYCEN, IXCEN for last annulus
C   RADMIN ...... Minimum distance from center for first annulus
C   RDELMN ...... Minimum allowed distance between annuli
C   RESID ....... Hot gas component
C   RFACTR ...... Factor used to determine the distance between annuli
C   ROTATE ...... Rotation of pie slices in degrees
C
C Perry Wood, Eric Feigelson
C Department of Astronomy, Penn State University
C February, 1984
C*************************************************************************
      CHARACTER*18 FILIN, FILOUT, PNAME
      INTEGER*2 NBOX(50,50), LBOX(50), IDATA(8)
      REAL*4 DATA(315,315), CTS(50,50), ANN(50), DENMIN(50)
      REAL*4 PHIMIN(50), R(50)
C
C . . . Initial parameters
C
```

```
      DATA NROWS, NCOLS, IYCEN, IXCEN /315, 315, 158, 158/
      DATA DELPHI, RADDEG, ROTATE /45., 57.29578, 20./
      DATA FILIN, FILOUT /'XRAY.DAT01', 'RESID.DAT02'/
      DATA RADMIN, RFACTR, RDELMN /5., 4., 1.5/
      DATA PNAME /'XSUB VSFOR'/
C
      R1MAX = (NROWS - IYCEN)
      R2MAX = (NCOLS - IXCEN)
      RADMAX = AMIN1(R1MAX,R2MAX)
      NPHI = INT(360. / DELPHI)
      DO 14 I = 1, 50
        DENMIN(I) = 1.0E20
        LBOX(I) = 0
        DO 16 J = 1, 50
          NBOX(I,J) = 0
          CTS(I,J) = 0.
   16   CONTINUE
   14 CONTINUE
C
C . . . Read in the data
C
      DO 10 I = 1, NROWS
        READ(21)(DATA(I,J), J = 1, NCOLS)
   10 CONTINUE
      READ(21)(IDATA(J), J = 1, 8)
C
C . . . Define annulus boundaries
C
      DO 100 IRAD = 1, 50
        IF(IRAD .EQ. 1)THEN
          ANN(IRAD) = RADMIN
        ELSE
          DELRAD = IRAD / RFACTR
          IF(DELRAD .LT. RDELMN)THEN
            DELRAD = RDELMN
          END IF
          ANN(IRAD) = ANN(IRAD-1) + DELRAD
        END IF
        IF(ANN(IRAD) .GT. RADMAX)THEN
          MAXANN = IRAD - 1
          MAXREG = MAXANN - 1
          GO TO 110
        END IF
  100 CONTINUE
C
C . . . Loop through the data array, and find in which radial and
C       azimuthal bin each (IY,IX) pixel belong.
C
  110 DO 200 IY = 1, NROWS
        DELY = IY - IYCEN
        DO 210 IX = 1, NCOLS
          DELX = IX - IXCEN
          DIST = SQRT(DELX**2 + DELY**2)
          DO 215 IRAD = 1, MAXREG
```

```
                IF(DIST .GE. ANN(IRAD)  .AND.  DIST .LT. ANN(IRAD+1))THEN
                  JRAD = IRAD
                  IF(DELY .LE. 0.0  .AND.  DELX .GT. 0.0)THEN
                    PHI = 270. - ATAN(DELY/DELX) * RADDEG + ROTATE
                  ELSE IF(DELY .GT. 0.0  .AND.  DELX .LT. 0.0)THEN
                    PHI = 90. - ATAN(DELY/DELX) * RADDEG + ROTATE
                  ELSE IF(DELY .GT. 0.0  .AND.  DELX .GT. 0.0)THEN
                    PHI = 270. - ATAN(DELY/DELX) * RADDEG + ROTATE
                  ELSE IF(DELY .LE. 0.0  .AND.  DELX .LT. 0.0)THEN
                    PHI = 90. - ATAN(DELY/DELX) * RADDEG + ROTATE
                  ELSE IF(DELY .GT. 0.0  .AND.  DELX .EQ. 0.0)THEN
                    PHI = 180. + ROTATE
                  ELSE IF(DELY .LE. 0.0  .AND.  DELX .EQ. 0.0)THEN
                    PHI = 0.0 + ROTATE
                  END IF
                  IF(PHI .GE. 360.)THEN
                    PHI = PHI - 360.
                  END IF
                  JPHI = INT(PHI / DELPHI + 1.)
C
C . . . Increment the count and area for bin (JRAD,JPHI)
C
                  CTS(JRAD,JPHI) = CTS(JRAD,JPHI) + DATA(IY,IX)
                  NBOX(JRAD,JPHI) = NBOX(JRAD,JPHI) + 1
                  LBOX(JRAD) = LBOX(JRAD) + 1
                END IF
  215       CONTINUE
  210     CONTINUE
  200   CONTINUE
C
C . . . Find and keep in array DENMIN(IRAD) the smallest count density
C       in each radial bin.
C
        WRITE(6,6010)PNAME, RFACTR, ROTATE, FILIN, RADMIN, RADMAX, FILOUT,
       &             IYCEN, IXCEN
        WRITE(6,6020)
        DO 300 IRAD = 1, MAXREG
          R(IRAD) = SQRT((ANN(IRAD)**2 + ANN(IRAD+1)**2) / 2.)
          DO 310 IPHI = 1, NPHI
            DENS = CTS(IRAD,IPHI) / NBOX(IRAD,IPHI)
            IF(DENS .LT. DENMIN(IRAD))THEN
              DENMIN(IRAD) = DENS
              PHIMIN(IRAD) = IPHI
            END IF
  310     CONTINUE
          WRITE(6,6000)IRAD, ANN(IRAD), ANN(IRAD+1), LBOX(IRAD),
     &                 PHIMIN(IRAD), DENMIN(IRAD), R(IRAD), R(IRAD)*4.,
     &                 DENMIN(IRAD)/16.
  300   CONTINUE
C
C . . . Subtract the hot gas component.
C
        DO 400 IY = 1, NROWS
          DELY = IY - IYCEN
```

```
            DO 410 IX = 1, NCOLS
              DELX = IX - IXCEN
              DIST = SQRT(DELX**2 + DELY**2)
              IF(DIST .GE. RADMIN  .AND.  DIST .LT. RADMAX)THEN
                IF(DIST .LT. R(2))THEN
                  I = 2
                ELSE IF(DIST .GE. R(MAXREG))THEN
                  I = MAXREG - 1
                ELSE
                  J = MAXREG - 1
                  DO 420 IRAD = 2, J
                    IF(DIST .GE. R(IRAD)  .AND.  DIST .LT. R(IRAD+1))THEN
                      I = IRAD
                    END IF
  420             CONTINUE
                END IF
                XX1 = DIST - R(I-1)
                XX2 = DIST - R(I)
                XX3 = DIST - R(I+1)
                X1X2 = R(I-1) - R(I)
                X1X3 = R(I-1) - R(I+1)
                X2X3 = R(I) - R(I+1)
                RESID = ((XX2 * XX3 * DENMIN(I-1)) / (X1X2 * X1X3)) -
     &                  ((XX1 * XX3 * DENMIN(I)) / (X1X2 * X2X3)) +
     &                  ((XX1 * XX2 * DENMIN(I+1)) / (X1X3 * X2X3))
                DATA(IY,IX) = DATA(IY,IX) - RESID
              END IF
  410       CONTINUE
            WRITE(20)(DATA(IY,IX), IX = 1, NCOLS)
  400   CONTINUE
        WRITE(20)(IDATA(J), J = 1, 8)
        STOP
C
 6000 FORMAT(2X, I2, 6X, F6.2, 6X, F6.2, 6X, I4, 6X, F3.1, 5X, F6.2,
     &       6X, F6.2, 6X, F7.2, 6X, F6.3)
 6010 FORMAT(5X, 'Program: ', A18, T45, 'RFACTR = ', F5.2, 4X,
     &       'ROTATE = ', F5.1, /, 5X, 'Input: ', A18, T45, 'RADMIN = ',
     &       F6.1, 3X, 'RADMAX = ', F6.1, /, 5X, 'Output: ', A18, T45,
     &       'IYCEN = ', I4, 6X, 'IXCEN = ', I4, //)
 6020 FORMAT(' IRAD     ANN(IRAD)  ANN(IRAD+1)   LBOX    PHIMIN', 4X,
     &       'DENMIN', 9X, 'R', 10X, 'R"', 4X, 'CNTS/SQ ARCSEC', /, 1X,
     &       98('='))
      END
//DATA.FT21F001 DD UNIT=DISK,VOL=REF=MEN.U67410.PW6.LIB,
// DSN=MEN.U67410.PW6.XRAY.DAT01,DISP=(OLD,KEEP),
// DCB=(RECFM=VBS,LRECL=200,BLKSIZE=4004)
//DATA.FT20F001 DD UNIT=DISK,VOL=REF=MEN.U67410.PW6.LIB,
// DSN=MEN.U67410.PW6.RESID.DAT02,DISP=(NEW,KEEP),
// DCB=(RECFM=VBS,LRECL=200,BLKSIZE=4004),
// SPACE=(TRK,(20,10),RLSE)
```

APPENDIX B

FORTRAN Program to Calculate a(n) and b(n)

```
//VO1XXXXX JOB
// EXEC FVCG
//SOURCE.SYSIN DD *
C*************************************************************************
C PROGRAM: ABCALC VSFOR
C
C PURPOSE: Calculate the values of a(n) and b(n) from RADIATION
C          PROCESSES IN ASTROPHYSICS, Tucker, equations 4-53 and 3-51.
C
C LOCAL VARIABLES:
C          A . . . . . a(n)
C          B . . . . . b(n)
C      ERROR . . . . . Desired accuracy of Riemann zeta function
C
C Perry Wood
C Department of Astronomy, Penn State University
C July, 1984
C*************************************************************************
      LOGICAL*1 RDATE(8)
      CHARACTER*8 WDATE
      CHARACTER*15 PNAME
      REAL*8 A, N, C, B, N1, AB, BA, ERROR
C
      DATA WDATE, PNAME, IVERS/'07/31/84', 'ABCALC VSFOR', 1/
      ERROR = 1.0D-6
      CALL DATE(RDATE)
      WRITE(6,604)PNAME, IVERS, WDATE, (RDATE(I), I = 1, 8), ERROR
      C = DSQRT(3.0D0) / (8.0 * DSQRT(3.141592653589793D0))
      WRITE(6,602)
C
      DO 10 N = 0.5, 5.1, 0.1
         A = 2**((N-1.)/2.) * C * DGAMMA((3. * N - 1.) / 12.)
     &      * DGAMMA((3. * N + 19.) / 12.) * DGAMMA((N + 5.) / 4.)
     &      / ((N + 1.) * DGAMMA((N + 7.) / 4.))
         N1 = 0.5 * (N + 5.0)
         CALL RIEMAN(N1, B, ERROR)
         B = B * 2.**(N+3.) * (N**2 + 4.*N + 11.) * DGAMMA(N1)
     &      / ((N + 3.)**2 * (N + 1.) * (N + 5.))
         AB = A / B
         BA = B / A
         WRITE(6,600)N, A, B, AB, BA
   10 CONTINUE
      STOP
C
  600 FORMAT(1X, F3.1, 4(3X, D12.5))
  602 FORMAT(16X, 'n', 8X, 'a(n)', 10X, 'b(n)', 9X, 'a(n)/b(n)', 6X,
     &       'b(n)/a(n)', /, 15X, '---', 7X, '----', 11X, '----', 9X,
     &       '---------', 6X, '---------')
```

```
  604 FORMAT(15X, 'Program: ', A15, 4X, 'Version: ', I2, 4X, 'Date: ',
     &       A8, /, 15X, 'Run: ', 8A1, /, 15X, 'Error:  < ', D8.3, //)
      END
C
C This section calculates the Riemann zeta function.  The sum is from
C zero to a cutoff point which is found by specifying the desired
C error.  The error is less than or equal to the integration of the
C series from the cutoff to infinity.
C
      SUBROUTINE RIEMAN(S, ANS, ERROR)
      REAL*8 S, ANS, ERROR, CUTOFF, XERROR
      CUTOFF = 0.0D0
   20 CUTOFF = CUTOFF + 100.
      XERROR = (CUTOFF**(1.0-S) / (S - 1.0)) + CUTOFF**(-S)
      IF(XERROR .GT. ERROR)GO TO 20
      M = DINT(CUTOFF)
      ANS = 0.0D0
      DO 10 K = 1, M
         ANS = ANS + 1.0 / DFLOAT(K)**S
   10 CONTINUE
      RETURN
      END
```